THE JOURNAL OF PHYSICAL CHEMISTRY C

Article

Cite This: J. Phys. Chem. C XXXX, XXX, XXX−XXX

pubs.acs.org/JPCC

Detecting DNA Methylation Using Surface-Enhanced Raman Spectroscopy

Syed Mohammad Abid Hasan,[†] Yuyang He,[‡] Te-Wei Chang,[§] Jianwei Wang,[‡] and Manas Ranjan Gartia*[,†]

[†]Department of Mechanical and Industrial Engineering and [‡]Department of Geology and Geophysics and Center for Computation and Technology, Louisiana State University, Baton Rouge, Louisiana 70803, United States

[§]Intel Corporation, Ronler Acres Campus, Hillsboro, Oregon 97124, United States

Supporting Information

ABSTRACT: Among all of the epigenetic events that are responsible for various diseases such as cancer, lupus, and several birth defects, DNA methylation is one of the crucial ones. It occurs because of the alkylation of various bases. These modifications of genes carried through altered creations of proteins ultimately lead to various diseases. For example, a vital cause behind canine lymphoma is found to be DNA methylation in the guanine base. In this work, we analyzed the methylated and nonmethylated guanine structure with the assistance of surface-enhanced Raman spectroscopy and density functional theory (DFT). Because of their vulnerability for causing DNA methylation, the N7 and O6 positions of the guanine structure were the positions of interest with the addition of various adducts such as methyl, hydroxyethyl, and deuterated methyl groups. To distinguish the methylated samples from the nonmethylated ones, principal component analysis was performed, and the same analysis was used to distinguish their methylated positions and added adducts. The experimental results were then explained by structure optimization and frequency calculation of the molecules based on DFT calculations. To understand the charge distribution and detect the possible locations of alkylation of DNA bases, electrostatic potential, highest occupied molecular orbital, and lowest unoccupied molecular orbital for each of the molecules were analyzed, and the reactivity was discussed in the light of electronic structure calculations. The results presented in this study demonstrate a potential label-free technique to examine epigenetic modification of DNA.

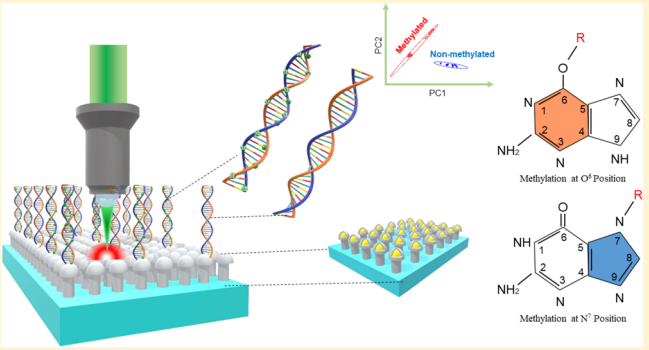

1. INTRODUCTION

Epigenetic mechanisms include various direct chemical modifications of DNA, which lead to varied gene appearance profiles in cells and tissues of multicellular organisms. DNA methylation is the conjugation of a methyl group to the DNA bases and is considered to be one of the most important epigenetic mechanisms.[1−6] Studying DNA methylation is important as it leads to hyper and/or hypo methylation of genes, which may cause suppression and/or overexpression of certain genes. Generally, these modifications of genes are followed by altered production of proteins that lead to diseases such as cancer. DNA methylation can occur in all four DNA bases, such as adenine (A), thymine (T), guanine (G), and cytosine (C). Several links have been found between DNA methylation and various diseases such as cancer,[7−10] lupus,[11−14] muscular dystrophy,[15,16] and numerous birth defects.[17,18] An example of agents responsible for methylation in the cells is *S*-adenosylmethionine. Various methylating agents found in the environment include methylmethane sulfonate, *N*-methyl-*N*′-nitro-*N*-nitrosoguanidine, and methyl halides.[19−22] Other sources of methylation are anticancer drugs such as chloroethylnitrosoureas and *N*-(2-chloroethyl)-*N*′-cyclohexyl-*N*-nitrosoureas. Some of these anticancer drugs can induce methylation (example includes carbazines such as pro- and da-carbazine, streptozotocine, and temozolomide); some of these drugs induce chloroethylation (example includes mustines such as lomustine, fotemustine, carmustine, and nimustine).[23,24] Nitrogen and oxygen atoms in the DNA bases are well-known sites for methylation.[25−27] Although multiple adducts are likely to formed due to agents responsible for alkylation, not all adducts can cause permanent DNA alteration. A methyl adduct on guanine is of particular interest because it causes mispairing and is associated with mutagenicity.[28−30] The preferred site for methylation is N7, which accounts for 70−90% of all adducts in guanine.[19,20,31] The O6 site accounts for about 6% of all adducts in guanine.[32] However, methylation of O6 position is found to be more mutagenic and more toxic compared to the methylation of N7 guanine position.[21,22] Furthermore, not all of the modifications of DNA bases lead to diseases as cells have mechanisms to

Received: October 18, 2018
Revised: December 12, 2018
Published: December 14, 2018

DOI: 10.1021/acs.jpcc.8b10178
J. Phys. Chem. C XXXX, XXX, XXX−XXX

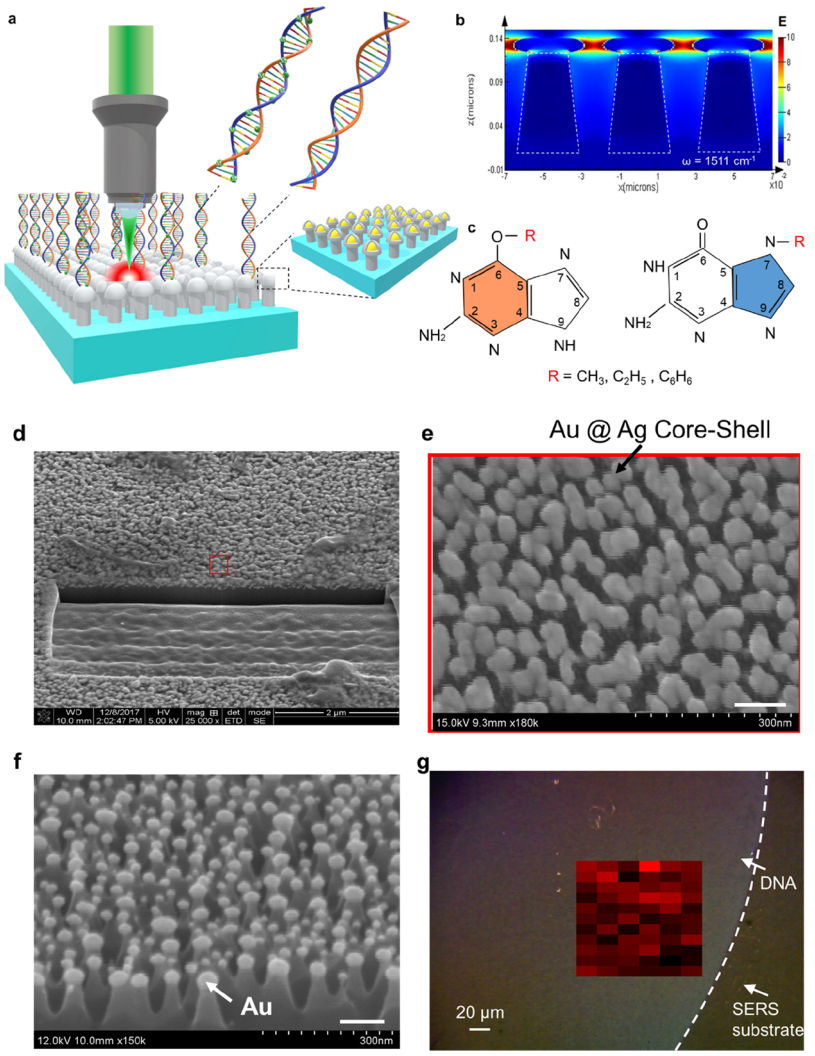

Figure 1. (a) Schematic showing the experimental setup of methylated and nonmethylated DNA attached to the Au@Ag core−shell SERS substrate. (b) Electromagnetic simulation showing Raman enhancement at 1511 cm^{-1} peak. (c) Chemical structures showing different adducts for guanine. (d,e) SEM image of the SERS substrate showing the Au@Ag core−shell structure on the silicon nanopillar. (f) Cross-sectional image of the SERS substrate before Ag deposition showing silicon nanopillar structures with Au nanoparticles on top. (g) Typical example of the Raman map for 1 nM N7 MG constructed at the 2119 cm^{-1} Raman band. The laser excitation wavelength was 633 nm.

repair the alterations.[33] The enzyme O6 methylguanine DNA methyltransferase (MGMT) directly repairs the adducts formed at the O6 guanine position. Although, MGMT primarily resides at the cytoplasm of the cells, during the DNA alkylation repair process, it translocates to the nucleus.[34] The MGMT protein repairs O6 methyl guanine (O6 MG) by transferring the methyl group from the O6 site of guanine to the Cys145 cysteine residue of MGMT.[35] In this process, the O6 guanine lesion is repaired but leads to the formation of *S*-methylcysteine. Such a process is irreversible and it inactivates the MGMT protein.[19,25,35,36] The MGMT protein undergoes ubiquitination after the reaction and prevents further interaction of the same protein molecule.[34] In addition to repairing the DNA damages in normal cells, MGMT repairing activity in cancer cells may also result in resistance to chemotherapeutic drugs.[37] Because of a close connection between methylation and cancer diseases, cell repair, and drug resistance, studying DNA methylation will provide a better understanding of the mechanism behind cancer drug resistance, which can lead to design better cancer drugs with fewer side effects and lower cytotoxicity.

Several experimental methods such as ultraviolet light-coupled high-performance liquid chromatography (HPLC-UV), methylation-specific polymerase chain reaction (PCR), bisulfite treatment, and DNA sequencing have been successfully utilized to detect DNA methylation. However, each of these techniques is associated with some limitations. HPLC-UV[38] usually requires a relatively large amount (3−10 μg) of DNA sample.[39] Methylation-specific PCR requires careful design of the primers as it is essential to discriminate between the methylated and nonmethylated molecules in bisulfite-treated DNA, as well as between bisulfite-converted DNA and DNA that is not converted during the bisulfite treatment.[40] In the bisulfite method, nonmethylated cytosine is converted to uracil,[41] and hence, it cannot be utilized to detect methylation of guanine. In addition, the sample preparation is often costly and time-consuming and extreme reaction conditions for the experiment sometimes lead to degradation of DNA.[42] Southern blot analysis requires high molecular weight DNA, and its accessibility is inadequate to restriction sites.[43] In contrast to those abovementioned techniques, surface-enhanced Raman spectroscopy (SERS) emerges as a novel

DOI: 10.1021/acs.jpcc.8b10178
J. Phys. Chem. C XXXX, XXX, XXX−XXX

technique to detect DNA methylation directly. SERS is capable of providing highly sensitive results even for multiplexed assays as the full width half-maximum of Raman vibration bands are narrow (~nanometer). In addition, SERS is label-free, and hence, photobleaching and blinking of fluorophores is not a concern.[44] Having the capability to detect label-free biomolecules, SERS is becoming popular for detecting single molecules such as DNA bases[45,46] and also for detecting DNA with single-base sensitivity.[47] Recently, SERS has been utilized to analyze single-base misalliances and base methylations in duplex DNA.[48] So far, SERS has been utilized to detect methylation of adenine[49] and more extensively of cytosine.[44,50−56] However, reported use of SERS to detect methylation of guanine is scarce. Here, we have utilized SERS to establish distinction between the methylated and nonmethylated form of guanine and to identify the position (N7 or O6) at where methylation happened. Principal component analysis (PCA) was used to analyze the large datasets of the SERS experiment for unsupervised data reduction.[57,58] Furthermore, to understand the vibrational spectroscopic features of guanine, density functional theory (DFT)-based electronic structure calculations were performed on six different isoforms of guanine. The DFT results explained experimental spectroscopic data. Taking together, the results demonstrated that using SERS to detect DNA methylation is a viable technique. Figure 1 portraits few key features of the entire study. Figure 1a schematically shows the experimental setup for methylated and nonmethylated DNA attached to the Au@Ag core−shell SERS substrate. Because of the laser illumination on the substrate, the localized surface plasmons will be excited on the SERS substrate. Figure 1b shows the electromagnetic simulation of the hot spot between two Au@Ag core−shell structures at a Raman frequency of 1511 cm^{-1}. The chemical structures of different adducts of guanine are shown in Figure 1c. Various adducts (denoted by R = CH_3, C_2H_5, C_6H_6) will be formed either at the O6 position (orange) or N7 position (blue) of the guanine. Figure 1d,e contains the scanning electron microscopy (SEM) image of the SERS substrate where the Au@Ag core−shell structure on the silicon nanopillar can be visualized, and Figure 1f shows the cross-sectional image of the SERS substrate before Ag deposition showing silicon nanopillar structures with Au nanoparticles on top. A typical Raman map for 1 nM N7 methyl guanine (N7 MG) constructed at the 2119 cm^{-1} Raman band is shown in Figure 1g. All of these key features will be explained in detail in the following sections of this paper.

2. EXPERIMENTAL SECTION

2.1. Materials. Guanine, O6 MG, N7 MG, O6-hydroxy ethyl guanine (O6 HEG), N7-2hydroxyethyl guanine (N7 2HEG), O6-benzyl guanine (O6 BG), and O6-methyl-*d*3-Guanine (O6 Md3G) were purchased from Sigma-Aldrich (St. Louis, MO, USA). To quantify adducts in the DNA samples, liquid chromatography followed by a mass spectrometry (LC/MS/MS)-based method was developed. Deuterated O6 methylguanine (O6 Md3G) was used as the internal standard. The standard curves for the LC/MS/MS experiments were generated by dissolving 0.1−10 ng of samples in methanol and adjusting the final volume to 150 μL by adding water. The mass of the internal standard (O6 Md3G) was maintained at 50 ng.

2.2. Preparation of the SERS Substrate. Microfabrication of the SERS substrate has been described in our earlier publications.[59,60] Briefly, a ⟨100⟩ p-type silicon 4 in. wafer coated with 6 nm Au was used for the thermal dewetting experiments. The Au-coated substrate underwent a rapid thermal annealing process at 500 °C for 1.5 min to form an island of Au nanoparticles. Subsequently, a reactive ion etching (RIE) process was utilized by using the Au nanoparticles as a mask to form nanopillar structures. Finally, 50 nm of Ag was deposited on those nanopillar structures using an e-beam evaporator for SERS properties.

2.3. LC/MS/MS Experiment. The samples were analyzed using a HPLC (1200 Series, Agilent Technologies, CA)-connected MS system (QTRAP 5500, AB Sciex, CA). The chromatographic separation was performed on an Agilent ZORBAX SB-Aq column (5 μm, 4.6 mm × 50 mm) while using 0.1% formic acid in water (phase A) and in acetonitrile (phase B) as mobile phases. A volumetric flow rate of 0.35 mL/min was used. The gradient was set to 100% A (0−1 min), 25% A (8−11 min), and 100% A (12−18 min). The electrospray ionization voltage was maintained at 5500 V. Multiple product ions were identified using multiple reaction monitoring for mass-to-charge (m/z) ratio of 70.1 through 312.2.

2.4. Sample Preparation for SERS Measurements. As mentioned in Materials section, different guanine adducts in powder form were purchased from Sigma-Aldrich (St. Louis, MO, U.S.A.) and were dissolved in Milli-Q water to prepare samples in the concentration range of 1 nM to 10 μM. To avoid further contamination, Milli-Q water was used for preparing the aliquot.

2.5. Raman Experiment and Data Analysis. The SERS spectra were acquired with a Renishaw inVia Raman Spectrometer with a 633 nm laser line. For each sample, 10 different locations were utilized to obtain the spectra. A 50× long working distance objective with a spot size of 1 μm × 1 μm, incident laser power of 50 mW, and exposure time of 10 s was utilized for each of the spectrum. Baseline correction and vector normalization were performed for each spectrum before multivariate analysis. OriginLab (Northampton, MA) was used for the preprocessing and PCA. The spectral data were first normalized and then smoothed by using the Savitzky−Golay method followed by PCA.

2.6. DFT Calculation. Gaussian 09 and Gaussview-05 software were used for the DFT calculations and analysis of the results. B3LYP density functional and 6-31G basis set were used to optimize the molecular geometries and calculate Raman spectra. MOLVIB[61−63] program was utilized for scaling the Raman intensities.

3. RESULTS AND DISCUSSION

3.1. SERS Enhancement Factor. Herein, we utilized a 3D Au@Ag core−shell nanopillar structure as a plasmonic substrate for analyzing the DNA. The 3D Au@Ag core−shell nanopillar structure was fabricated using thermal dewetting of a thin layer (6 nm) of gold, followed by rapid thermal annealing at 500 °C to make a nanoisland of gold (Figure S1). These gold nanoparticles were used as a mask to etch the underneath silicon using the RIE process (Figure S1). The Au@Ag core−shell structure was formed by depositing 50 nm of Ag after the formation of the nanopillar structure (Figures S2 and S3). The Au@Ag core−shell structure provides a 1000× higher SERS enhancement factor (EF) compared to the Au-based SERS substrate (Figure S3). The DNA adducts are conjugated to the Ag metal layer through the amino (−NH)

DOI: 10.1021/acs.jpcc.8b10178
J. Phys. Chem. C XXXX, XXX, XXX−XXX

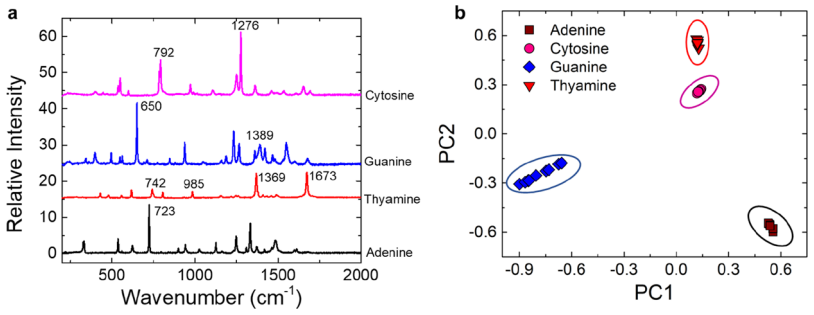

Figure 2. (a) SERS spectra (background-corrected) of DNA nucleobases [adenine (A), cytosine (C), guanine (G), and thymine (T)] adsorbed on the 3D Au@Ag core−shell SERS substrate. Excitation laser wavelength: 633 nm, incident laser power: 2 mW, exposure time: 10 s, and concentration: 1 nM were used to acquire the spectrum. (b) PCA plot (PC1 vs PC2) for the DNA base SERS spectra based on spectral intensities.

group of the molecules. This was experimentally verified from the SERS and normal Raman scattering (RS) spectra of guanine (Figure S4) where a strong band can be found for the normal RS spectrum of guanine at 3161 cm^{-1} but not present in the SERS spectrum of guanine. The 3161 cm^{-1} Raman band is generally associated with amino (−NH) group[64,65] stretching vibration of guanine. After adsorption to the Ag metal surface in the SERS experiment, the vibrational mode is absent in the SERS spectra. The SERS substrate provides intense electromagnetic hot spots at the junction between two core−shell structures (Figure S5). In addition to the electromagnetic enhancement, the metal−molecule conjugate will experience charge-transfer enhancement. In the current configuration, the Fermi energy level of Ag (−4.3 eV)[66] will reside between the highest occupied molecular orbital (HOMO) energy level (−6.049 eV) and lowest unoccupied molecular orbital (LUMO) energy level (−0.856 eV) of the guanine molecule. Because the energy of photon excitation used in this study (λ_{ex} = 633 nm or 1.96 eV) is not sufficient to make the transition of the electron from the Fermi level to the LUMO level of the molecule, most likely, the excited electron will be transferred from the HOMO level of the molecule to the Fermi level of Ag. Hence, charge transfer will take place from the molecule to the metal for achieving the surface-enhanced Raman signals. The experimental SERS EF of the substrate was estimated using the expression, $EF = \frac{I_{SERS} \times N_{bulk}}{I_{bulk} \times N_{SERS}}$, where I_{SERS} and I_{bulk} are the SERS intensity estimated for the 1511 cm^{-1} Raman band (assigned to aromatic C−C stretching modes of R6G on the SERS substrate and in bulk solution, respectively). $N_{bulk} = n_{bulk} \times N_A = C_{bulk} \times V_{bulk} \times N_A$ is the total number of molecules in the bulk solution used for the normal Raman measurement. $N_{SERS} = n_{SERS} \times N_A = C_{SERS} \times V_{SERS} \times N_A$ is the estimated number of molecules for the SERS measurement. Here, n_{bulk} and n_{SERS} are the amount in mole of R6G molecules in the scattering volume; V_{bulk} and V_{SERS} are the scattering volume (we keep the scattering volume same by dropping the same volume of droplet, $V_{bulk} = V_{SERS}$); C_{bulk} and C_{SERS} are the concentration of R6G in the bulk solution and SERS substrate, respectively. In our experiment (Figure S6), C_{bulk} = 100 mM and C_{SERS} = 100 nM. Hence, $= \frac{I_{SERS} \times C_{bulk}}{I_{bulk} \times C_{SERS}} = \frac{2057 \times 100 \times 10^{-3}}{20 \times 100 \times 10^{-9}} = 1.02 \times 10^8$.

3.2. SERS of DNA Bases. The reproducibility of the SERS substrate was checked by mapping of the Raman spectrum at different concentrations of guanine adducts (Figures S7 and S8). The Raman intensities are fairly uniform with ±15% variations. Because of the intense electromagnetic field and reproducible SERS signal, the challenging task of the direct detection of guanine isoforms becomes possible. Guanine with different methylation patterns was designed. For each of the methylated and nonmethylated guanine, 10 independent spectra were obtained. Baseline correction and vector normalization for each spectrum were followed by multivariate analysis. On the basis of PCA, discrimination between methylated and nonmethylated as well as the types of methylation was studied. To test the approach, the algorithm was utilized to detect single DNA bases (A, T, G, and C) from the Raman spectrum. For this experiment, picomole quantities of adenine, guanine, thymine, and cytosine are absorbed onto the SERS substrate. Characteristic band or bands of each DNA base such as the 723 cm^{-1} band for adenine (ring breathing mode),[67] 650 cm^{-1} band for guanine (ring breathing mode), 1389 cm^{-1} (ring stretching mode C−N, C−C),[68] 1369 cm^{-1} (in plane bending of N−H, C−H), and 1673 cm^{-1} (C═O stretching, asymmetric bending of N−H, C−H) for thymine,[69] and 1276 cm^{-1} (C−N ring stretching mode) and 792 cm^{-1} (ring breathing mode)[58] for cytosines are clearly identified (Figure 2a).

3.3. PCA Analysis of DNA Bases. PCA was utilized to reduce the dimension of large spectral arrays and to improve the identification of DNA bases from the spectral variances. The background was first removed by polynomial baseline correction method. Two different normalization methods, min−max and vector normalization, were applied after baseline correction. Then, high-frequency noises were removed through the Savitzky−Golay smoothing method. Because changes in the intensity of bands after DNA adduct formation are expected, we found that the min−max method is not appropriate for our application as it scaled all maximum peak values of each spectrum to 1. Then, PCA was applied on the smoothed spectrum and its first and second derivatives over the range of 200−3200 cm^{-1}. Finally, hierarchical cluster analysis (HCA) was performed on the PCA-reduced data for further classification and data presentation.

Figure 2b shows the PCA plot (PC1 vs PC2) for the SERS spectra of A, T, G, and C based on spectral intensities. We choose PC1 and PC2 because they exhibit the highest percentage variances among all principal components. The ellipse around the clustered group shows the 95% confidence limit of the PCA distribution. Hence, these elliptical rings signify the distance between the clusters of different DNA bases (A, T, G, and C). They can be utilized to quantify the specificity and reproducibility of the multivariate analysis method as well as the SERS substrate. As the results shown in

DOI: 10.1021/acs.jpcc.8b10178
J. Phys. Chem. C XXXX, XXX, XXX−XXX

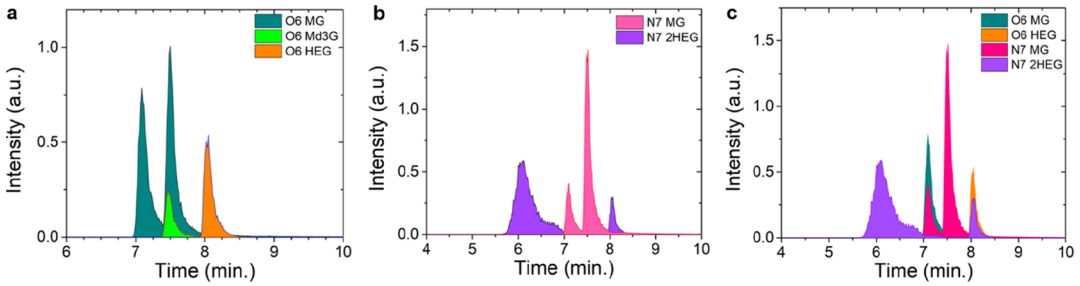

Figure 3. HPLC chromatogram of different guanine adducts showing (a) O6 MG, O6 Md3G, O6 2HEG, (b) N7 MG, N7 2HEG, (c) O6 MG, O6 2HEG, N7 MG, and N7 2HEG.

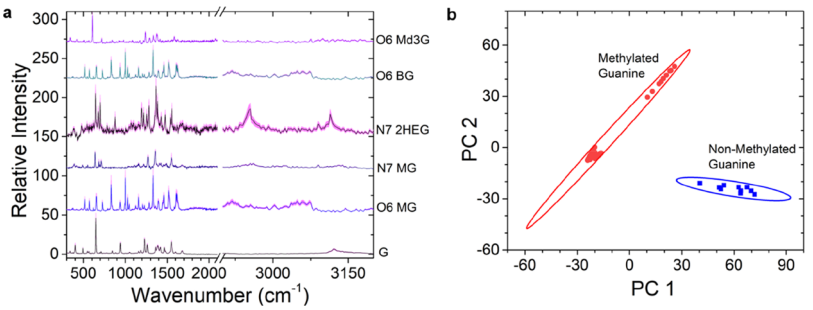

Figure 4. (a) Comparison of experimental SERS spectra (background-corrected and normalized) of guanine and its adducts. Excitation laser = 633 nm, incident power = 2 mW, integration time = 10 s, concentration = 1 nM. For clarity, the spectrums are offset by a constant quantity. The standard deviation of the spectrum collected from 10 different locations of the SERS substrate is represented by the pink band. (b) PCA plot (PC1 vs PC2) of SERS spectra based on spectral intensities of all methylated and nonmethylated guanine bases.

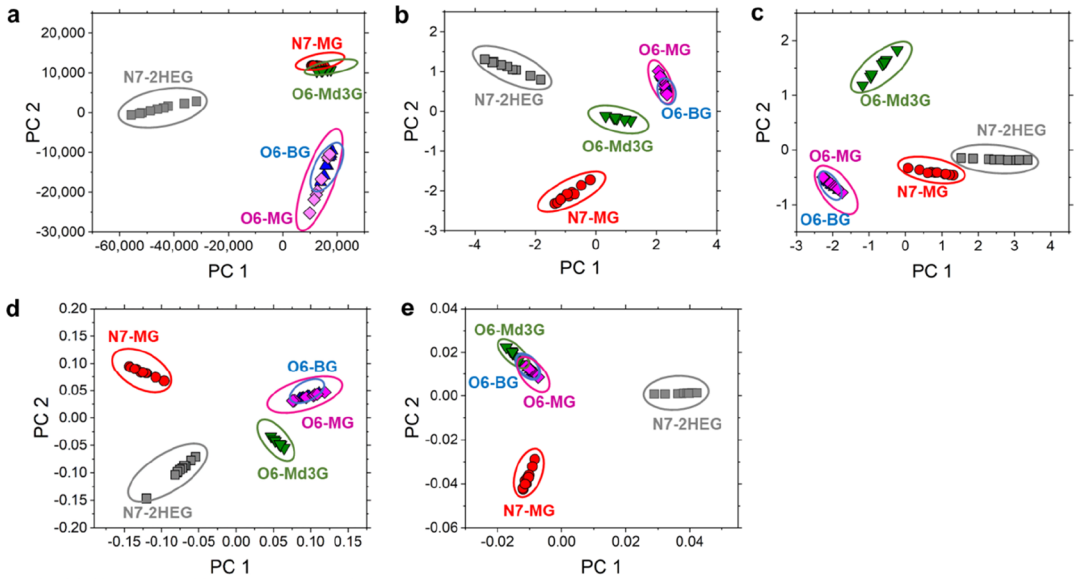

Figure 5. PCA plots (PC1 vs PC2) and clustering results of SERS spectra of O6 MG, N7 2HEG, N7 MG, O6 BG, and O6 Md3G based on (a) spectral intensities, (b) normalized spectral intensities, (c) normalized spectral intensities after applying the Savitzky–Golay smoothing method, (d) first-derivative spectra, and (e) second-derivative spectra. Each cluster ring shows 95% confidence interval.

Figure 2b, the clusters for different DNA bases are well separated.

3.4. Liquid Chromatography/Mass Spectrometry. To detect and quantify the guanine adducts, the LC/MS/MS method was used. Figure 3a shows typical chromatograms obtained for O6 MG, O6 HEG, and O6 Md3G. The corresponding chromatogram for N7 MG and N7 2HEG is shown in Figure 3b. The comparison of chromatograms obtained for all the abovementioned guanine adducts is shown in Figure 3c. There is substantial overlap between O6 MG and N7 MG (Figure 3c) chromatograms. Hence, HPLC alone cannot reliably separate all of the guanine adducts.

3.5. PCA Analysis of DNA Adducts. We set our objective to study (1) distinction between methylated guanine from nonmethylated guanine and (2) separation of types of adducts formed on the guanine. We want to classify each DNA adducts based on the SERS data using the PCA algorithm developed and implemented in Figure 2. Figure 4a shows the Raman spectra obtained from the SERS experiment for the non-methylated and methylated guanine samples—N7 2HEG, N7

DOI: 10.1021/acs.jpcc.8b10178
J. Phys. Chem. C XXXX, XXX, XXX−XXX

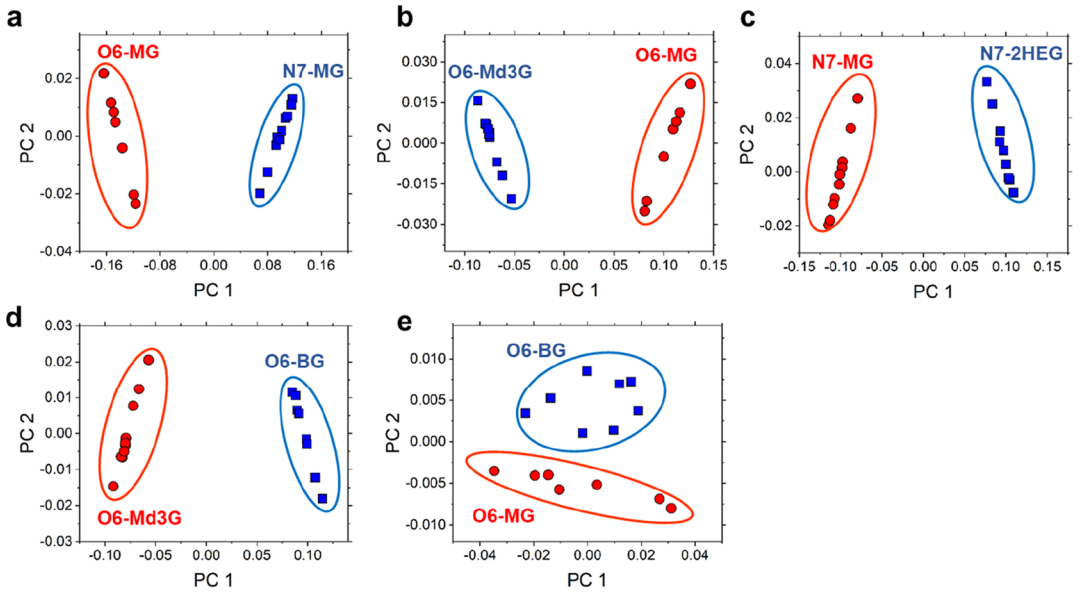

Figure 6. Pairwise comparison showing the PCA plots (PC1 vs PC2) based on the first derivative of normalized and smooth SERS spectra of (a) O6 MG vs N7 MG, (b) O6 Md3G vs O6 MG, (c) N7 MG vs N7 2HEG, (d) O6 Md3G vs O6 BG, and (e) O6 MG vs O6 BG.

MG, O6 Md3G, O6 BG, and O6 MG. The important vibrational modes for all of the spectra have been identified and tabulated in the Supporting Information (Tables S3 and S4). Each spectrum has been taken from 10 different locations, and the pink thick line represents the standard deviations of all spectra. The PCA was carried out for all Raman frequency data, and the results were used to separate methylated DNA from the nonmethylated ones. Figure 4b shows that PCA can be successfully utilized to distinguish methylated and non-methylated DNA. PCA results of SERS spectra on spectral intensities of guanine adducts (O6 MG, N7 MG, O6 BG, N7 2HEG, and O6 Md3G) are shown in Figure 5a. The PC1 versus PC2 cluster showed substantial overlap. The HCA dendrogram (Figure S9) shows that the DNA adducts cannot be classified separately. To improve the classification, PCA was performed on post processed data including vector normalized (Figure 5b), filtered (Figure 5c), first-derivative (Figure 5d), and second-derivative (Figure 5e) spectra. As shown in Figure 5, normalized and second derivative spectra were not successful in achieving segregation of clusters (also shown in HCA dendograms). In contrast, the first-derivative spectrum was mostly successful (except O6 MG and O6 BG) in exhibiting segregation of clusters. Hence, for the subsequent pairwise classification, the first-derivative method was used. Figure 6 shows that the first derivative-based input vectors for the PCA treatment of the DNA adducts consistently provided the best clustering results. The pair wise clusters for O6 MG and N7 MG (Figure 6a), O6 Md3G and O6 MG (Figure 6b), N7 MG and N7 2HEG (Figure 6c), O6 Md3G and O6 BG (Figure 6d), and O6 MG and O6 BG (Figure 6e) are found to be well defined and separated from each other.

3.6. Loading Spectra for DNA Adducts. The loadings or spectral features responsible for the PCA sources provide vital information of the characteristic features of each molecule. Figure 7 shows the loading plot of methylated samples based on the PCA treatment. Significant peaks are highlighted through which it can be explained why each of the datasets is different from the others. A characteristic peak such as the 1554 cm^{-1} band was found for both N7 MG and N7 2HEG

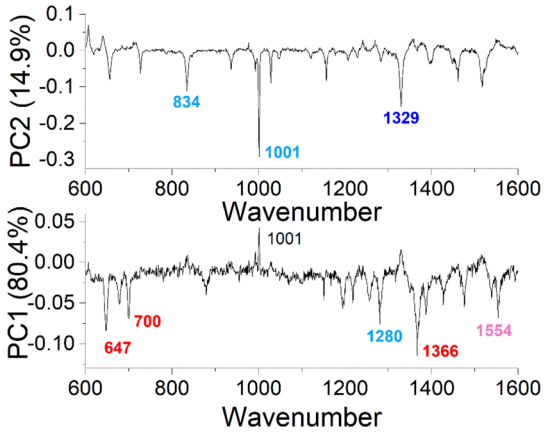

Figure 7. Loading spectra for the first and second principal components identifying important Raman frequencies to distinguish different DNA adducts. The numbers with different colors signify a particular DNA adduct. Red (N7 2HEG), blue (O6 BG and O6 MG), pink (N7 MG), and deep blue (O6 MG, O6 BG, and O6 Md3G).

samples but did not appear in other methylated samples. From the DFT calculation, this band (1554 cm^{-1}) is found to be associated with $-NH_2$ and CH_3 scissoring, symmetric stretching of (C8−N9), (C4−N3), (C2−N1), (N3−C4), and (C4−C5), and in plane deformation of (N1−H). Similarly, 647 cm^{-1} (pyrimidine and imidazole breathing mode), 700 cm^{-1} (C═O in plane deformation; pyrimidine and imidazole stretching; and CH_2 twisting), and 1366 cm^{-1} (CH_2 wagging) bands were found only in N7 2HEG; thus, N7 2HEG can be distinguished from N7 MG and N7 2HEG mixture samples based on the appearance of 647, 700, and 1366 cm^{-1} characteristic Raman peaks. The 1323 cm^{-1} band was found only in the O6 methylated positions of guanine (O6 MG, O6 Md3G, and O6 BG) samples and did not appear in the N7 MG and N7 2HEG samples, and 834, 100, 1001, and 1280 cm^{-1} bands were common in O6 MG and O6 BG but did not appear in O6 Md3G samples.

DOI: 10.1021/acs.jpcc.8b10178
J. Phys. Chem. C XXXX, XXX, XXX−XXX

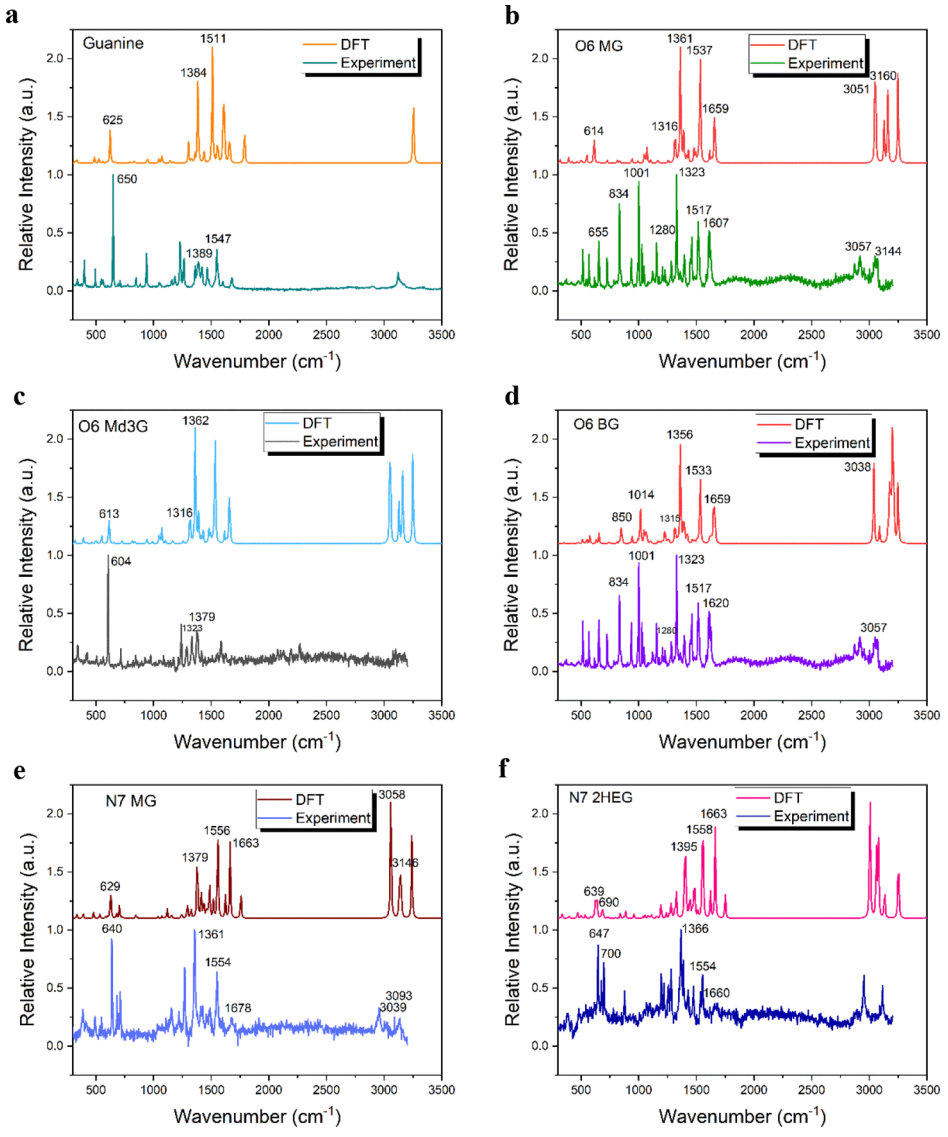

Figure 8. Comparison of the experimental Raman spectrum of the DNA adducts with that of DFT results for (a) G, (b) O6 MG, (c) O6 Md3G, (d) O6 BG, (e) N7 MG, and (f) N7 2HEG.

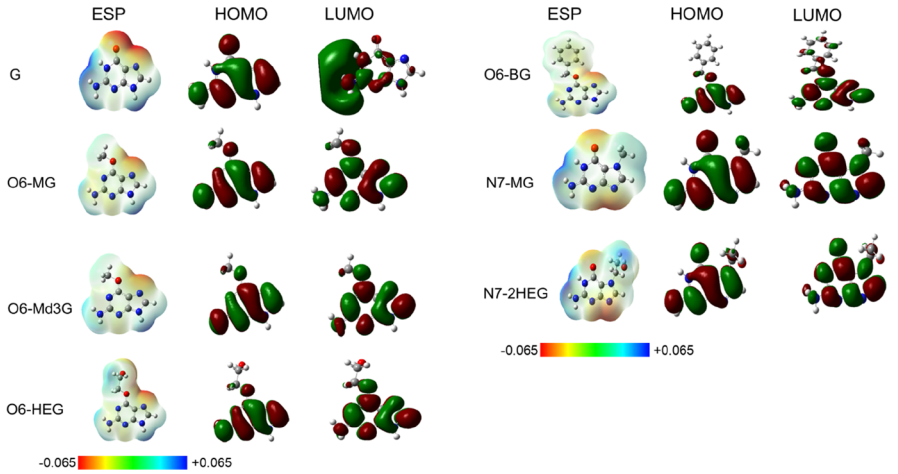

Figure 9. Plot showing MEP and the HOMO and LUMO energy levels for methylated and nonmethylated guanine.

3.7. Comparison of Experimental and Computational Raman Spectra. To assign the fundamental vibrational modes of guanine and its adducts in the SERS experiments, DFT calculations have been performed. Figure 8 shows the

DOI: 10.1021/acs.jpcc.8b10178
J. Phys. Chem. C XXXX, XXX, XXX−XXX

Table 1. Global Reactivity Descriptor of Guanine and Its Adducts

molecular properties	G	O6 MG	O6 Md3G	O6 HEG	O6 BG	N7 MG	N7 HEG
E_{HOMO} (eV)	−6.049	−5.866	−5.865	−5.888	−5.904	−6.043	−6.007
E_{LUMO} (eV)	−0.856	−0.718	−0.717	−0.745	−0.788	−1.015	−0.988
$\Delta E_{HOMO-LUMO}$ (eV)	5.193	5.148	5.148	5.143	5.117	5.028	5.019
ionization potential, I (eV)	6.049	5.866	5.865	5.888	5.904	6.043	6.007
electron affinity, A (eV)	0.856	0.718	0.717	0.745	0.788	1.015	0.988
electronegativity, χ (eV)	3.452	3.292	3.291	3.317	3.346	3.529	3.497
chemical potential, μ (eV)	−3.452	−3.292	−3.291	−3.317	−3.346	−3.529	−3.497
chemical hardness, η (eV)	2.596	2.574	2.574	2.572	2.558	2.514	2.509
chemical softness, s (eV^{-1})	0.193	0.194	0.194	0.194	0.195	0.199	0.199
global electrophilicity index, ω (eV)	2.295	2.105	2.104	2.139	2.188	2.477	2.437

comparison of experimental Raman spectra of the DNA adducts with those of DFT results. For guanine, the major peaks appear at around 650 cm^{-1} and in the range of 1200−1700 cm^{-1} for both DFT and experimental results (Figure 8a). The similarity between DFT and experimental Raman spectra shows that the DFT-calculated Raman spectrum can be representative for guanine. Also, the relative high intensities in the range of 1200−1700 and 2800−3200 cm^{-1} for O6 MG (Figure 8b), O6 Md3G (Figure 8c), O6 BG (Figure 8d), N7 MG (Figure 8e), and N7 2HEG (Figure 8f) are comparable between DFT and experimental spectra. The corresponding detailed band assignments are provided in the Supporting Information (Tables S3 and S4). The computed Raman frequencies compare well with the experimental results, although there are systematic shifts between the peak frequencies because of the well-documented systematic errors of the DFT methods.[70,71] The calculated intensities have some differences as compared to the experimental results. The main reason for this is that the computed results correspond to isolated molecules at 0 K, whereas the experimental results are for the solid-state molecules at room temperature.

3.8. Chemical Reactivity Analysis of DNA Adducts. Figure 9 shows the plot of the molecular electrostatic potential (MEP), HOMO, and LUMO for guanine and methylated isoforms of guanine. The electrostatic plot of guanine shows a high electron density to be localized around the oxygen (O6) atom of the pyrimidine ring and the nitrogen (N7) atom of the imidazole ring. Therefore, O6 and N7 positions of guanine are the most nucleophilic and reactive sites (marked in red color) of the guanine structure where most of the adducts are generally formed. Different colors of the MEP surface represent different values of electrostatic potential. Red color represents the most negative, blue color represents the most positive, and green color represents the zero electrostatic potential. The negative MEP surfaces (shades of red and yellow) correspond to attraction of a proton by the nuclei and are possible sites for electrophilic attack (e.g., drug metabolites, pollutants, and heavy metals). The positive MEP surfaces (shades of blue) are localized over the hydrogen atoms and are possible sites for nucleophilic attack (e.g., biological targets like the cysteine residue, Cys145 of the MGMT protein). MEP descriptors are useful to predict biological activity that relies on noncovalent (electrostatic) interactions. To describe the local and global chemical reactivity of the molecule, frontier molecular orbitals (FMOs) are useful. The HOMO and LUMO energy levels are also characteristics of the ionization potential (electron-donating capability) and the electron affinity (electron-accepting capability) of the molecule. As shown in Figure 9, there is a general similarity in the HOMO between guanine and methylated isoforms of guanine, which suggests that chemical bonding characters only slightly change after methylation except for O6-BG. In contrast, there are significant differences in the LUMO among different methylated isoforms, suggesting that different methylation may cause different chemistries of these isoforms. The global reactivity descriptor of the guanine adducts is shown in Table 1. With higher HOMO energy level, O6 MG is a better electron donor compared to N7 MG. A large HOMO−LUMO gap represents large chemical hardness and less reactive molecules. Among the guanine adducts, O6 MG has the highest HOMO−LUMO gap and N7 MG as well as N7 HEG has the lowest HOMO−LUMO gap. Therefore, N7 MG is expected to be more readily formed compared to O6 MG. In fact, under *in vitro* and *in vivo* conditions, it has been observed that alkylation of N7 position of guanine occurs more frequently compared to O6 position.[72,73] The LUMO energy level of the molecules can also be utilized to predict the likelihood of alkylation through nitrosourea compound (e.g., chemotherapy drugs). According to the FMO theory, the greater the HOMO−LUMO overlap between molecules, the better is the reaction. Hence, the closer the HOMO energy level of guanine (biological target) to the LUMO energy level of the electrophile [toxicants or drugs like *N*-ethyly-*N*-nitrosourea (ENU) or *N*-methyl-*N*-nitrosourea (MNU)], the higher will be the relative reactivity of the toxicant. For example, LUMO of ENU (−2.309 eV)[74] is lower compared to LUMO of MNU (−0.681 eV).[75] Therefore, ENU can form an adduct with guanine more readily compared to MNU, which is also observed experimentally.[72,76,77] The LUMO energy level is also useful in predicting the mutagenicity of the guanine adduct. Because N7 MG's LUMO energy level (−1.015 eV) is closer to the HOMO energy level of MGMT, compared to O6 MG's LUMO energy level (−0.718 eV), N7 MG will readily react with MGMT. Because MGMT is a repair gene which will remove the methyl group, it is expected that N7 MG is less mutagenic. Experimental data support that O6 MG is more mutagenic than N7 MG, although N7 MG is more readily formed.[19−22,25,72,78] Using Koopman's theorem, other global reactivity indices such as electronegativity ($\chi = (I + A)/2$), chemical potential ($\mu = -X$), chemical hardness ($\eta = (I - A)/2$), chemical softness ($s = 1/2\eta$), and global electrophilicity index ($\omega = \mu^2/2\eta$) can be estimated from the HOMO and LUMO energy values. Table 1 lists the estimated values of these global reactivity indices. Chemical potential describes the electron donation tendency of a molecule at a constant potential and it is the opposite of electronegativity. Similarly, chemical hardness is the resistance of chemical species to undergo electron transfer and a hard molecule is more stable.

DOI: 10.1021/acs.jpcc.8b10178
J. Phys. Chem. C XXXX, XXX, XXX−XXX

Table 2. Polarizability of Guanine and Its Adducts

molecule	α_{xx} (a.u)	α_{yy} (a.u.)	α_{zz} (a.u.)	$\langle\alpha\rangle$ (a.u.)	p (total dipole moment) (a.u.)
G	137.20	111.29	54.44	100.97	302.93
N7 MG	151.52	125.22	63.26	113.33	340.00
O6 MG	151.51	129.70	64.57	115.56	345.78
O6 Md3G	151.51	129.70	64.57	115.56	345.78
N72HEG	168.78	138.99	82.77	130.18	390.54
O6 HEG	158.21	161.11	81.17	133.50	400.49
O6 BG	242.28	212.50	106.79	187.19	561.57

From the table, O6 MG is more stable than N7 MG. The global electrophilicity index describes the affinity of the molecule to accept electrons. Hence, molecules with high global electrophilicity index are good electrophiles. It can be inferred from Table 1 that N7 MG is a good electrophile and O6 MG is a nucleophile compared to N7 MG.[79] Other electrical properties for the quantitative structure−activity relationship models are dipole moment and polarizability. Dipole moment is a measure of likelihood of electrostatic interaction near the molecule. For example, it can be utilized to estimate diffusion across a lipid bilayer or predict host−guest interaction (electrostatic binding) of a ligand at the active site of a protein.[35] A large dipole moment usually signifies favorable energy of hydration. One caveat of using dipole moment as a predictor of molecule−molecule interaction is that it is highly dependent on the conformation of the molecule, and in a biological system, the molecular conformation dynamically changes. Further, polarizability can be utilized to compare the reactivity among guanine adducts varying with carbon chain length at a particular location. O6 HEG and O6 BG have the highest polarizability among all adducts and hence they will be more reactive compared to others. This trend based on the basic properties of the molecules is consistent with an experimental observation where it showed stronger preference for reaction at O6 position for larger alkyl group.[72] Among the adducts at the N7 position, polarizability of N7 2HEG is greater than that of N7 MG. Thus, N7 2HEG is expected to be more reactive and N7 MG will be relatively stable compared to N7 2HEG. The half-lives of N7 MG and N7 2HEG were experimentally found to be 150 and 50 h[80−83] under physiological pH conditions, respectively, which are in agreement with our theoretical predictions (Table 2).

4. CONCLUSIONS

The detection of methylation in DNA was carried out successfully by using the SERS technique. Statistical analysis of the spectra is critical to distinguish different methylated samples based on their adducts and their methylated positions. Structure optimization and Raman frequency calculations based on DFT are essential for the interpretation of the spectra and the understanding of methylation. The differences between methylated and nonmethylated samples are better understood based on the results of analyzing the electrostatic potential and HOMO−LUMO. Integration of SERS, statistical analysis, and theoretical calculations demonstrates a feasible, label-free technique to effectively detect the presence of a methyl adduct on DNA.

■ ASSOCIATED CONTENT

Supporting Information

The Supporting Information is available free of charge on the ACS Publications website at DOI: 10.1021/acs.jpcc.8b10178.

Schematic of the Au@Ag core−shell nanopillar structure fabrication process; calculation of SERS EF; comparison of SERS enhancement obtained from the Au structure and Au@Ag core−shell structure; Raman mapping images of guanine adducts on the SERS substrate; FDTD simulation showing the electromagnetic hot spots at the junction between two core−shell structures of the SERS substrate; chemical structures of different guanine adducts; table showing the significant Raman peaks for guanine and its various adducts; table showing the description of the vibrational modes of guanine and its various adducts; and table for the bond length and angle for guanine and its various adducts (PDF)

■ AUTHOR INFORMATION

Corresponding Author

*E-mail: mgartia@lsu.edu.

ORCID

Syed Mohammad Abid Hasan: 0000-0001-6546-8075
Yuyang He: 0000-0003-3220-1432
Jianwei Wang: 0000-0001-7671-0533
Manas Ranjan Gartia: 0000-0001-6243-6780

Notes

The authors declare no competing financial interest.

■ ACKNOWLEDGMENTS

We acknowledge the support from the Louisiana Board of Regents Support Fund (contract number: LEQSF(2017-20)-RD-A-04 and LEQSF(2017-18)-ENH-TR-08) and National Science Foundation (NSF award number: 1660233). SEM and Raman spectroscopy was performed at the shared instrumentation facility (SIF) at Louisiana State University. The computation used resources of the National Energy Research Scientific Computing Center, a DOE Office of Science User Facility supported by the Office of Science of the U.S. Department of Energy under contract no. DE-AC02-05CH11231. Portions of the computation were conducted with high-performance computing resources provided by Louisiana State University (http://www.hpc.lsu.edu).

■ REFERENCES

(1) Avery, O. T.; MacLeod, C. M.; McCarty, M. Studies on the chemical nature of the substance inducing transformation of pneumococcal types: Induction of transformation by a desoxyribonucleic acid fraction isolated from pneumococcus type III. *J. Exp. Med.* **1944**, *79*, 137.

DOI: 10.1021/acs.jpcc.8b10178
J. Phys. Chem. C XXXX, XXX, XXX−XXX

(2) Hotchkiss, R. D. The quantitative separation of purines, pyrimidines, and nucleosides by paper chromatography. *J Biol Chem* **1948**, *175*, 315−332.
(3) Compere, S. J.; Palmiter, R. D. DNA methylation controls the inducibility of the mouse metallothionein-I gene in lymphoid cells. *Cell* **1981**, *25*, 233−240.
(4) Holliday, R.; Pugh, J. DNA modification mechanisms and gene activity during development. *Science* **1975**, *187*, 226−232.
(5) Moore, L. D.; Le, T.; Fan, G. DNA methylation and its basic function. *Neuropsychopharmacology* **2012**, *38*, 23−38.
(6) Baylin, S. B.; Mufti, G. J. Introduction. *Nat. Rev. Clin. Oncol.* **2005**, *2*, S1.
(7) Ehrlich, M. DNA methylation in cancer: Too much, but also too little. *Oncogene* **2002**, *21*, 5400.
(8) Herman, J. G.; Merlo, A.; Mao, L.; Lapidus, R. G.; Issa, J.-P. J.; Davidson, N. E.; Sidransky, D.; Baylin, S. B. Inactivation of the CDKN2/p16/MTS1 gene is frequently associated with aberrant DNA methylation in all common human cancers. *Cancer Res.* **1995**, *55*, 4525−4530.
(9) McCabe, M. T.; Brandes, J. C.; Vertino, P. M. Cancer DNA methylation: Molecular mechanisms and clinical implications. *Clin. Cancer Res.* **2009**, *15*, 3927−3937.
(10) Widschwendter, M.; Siegmund, K. D.; Müller, H. M.; Fiegl, H.; Marth, C.; Müller-Holzner, E.; Jones, P. A.; Laird, P. W. Association of breast cancer DNA methylation profiles with hormone receptor status and response to tamoxifen. *Cancer Res.* **2004**, *64*, 3807−3813.
(11) Coit, P.; Jeffries, M.; Altorok, N.; Dozmorov, M. G.; Koelsch, K. A.; Wren, J. D.; Merrill, J. T.; McCune, W. J.; Sawalha, A. H. Genome-wide DNA methylation study suggests epigenetic accessibility and transcriptional poising of interferon-regulated genes in naïve CD4+ T cells from lupus patients. *J. Autoimmun.* **2013**, *43*, 78−84.
(12) Javierre, B. M.; Fernandez, A. F.; Richter, J.; Al-Shahrour, F.; Martin-Subero, J. I.; Rodriguez-Ubreva, J.; Berdasco, M.; Fraga, M. F.; O'Hanlon, T. P.; Rider, L. G.; Jacinto, F. V.; Lopez-Longo, F. J.; Dopazo, J.; Forn, M.; Peinado, M. A.; Carreno, L.; Sawalha, A. H.; Harley, J. B.; Siebert, R.; Esteller, M.; Miller, F. W.; Ballestar, E. Changes in the pattern of DNA methylation associate with twin discordance in systemic lupus erythematosus. *Genome Res.* **2009**, *20*, 170−179.
(13) Richardson, B.; Scheinbart, L.; Strahler, J.; Gross, L.; Hanash, S.; Johnson, M. Evidence for impaired T cell DNA methylation in systemic lupus erythematosus and rheumatoid arthritis. *Arthritis Rheumatol.* **1990**, *33*, 1665−1673.
(14) Yung, R. L.; Quddus, J.; Chrisp, C. E.; Johnson, K. J.; Richardson, B. C. Mechanism of drug-induced lupus. I. Cloned Th2 cells modified with DNA methylation inhibitors in vitro cause autoimmunity in vivo. *J. Immunol.* **1995**, *154*, 3025−3035.
(15) Acharyya, S.; Sharma, S. M.; Cheng, A. S.; Ladner, K. J.; He, W.; Kline, W.; Wang, H.; Ostrowski, M. C.; Huang, T. H.; Guttridge, D. C. TNF inhibits Notch-1 in skeletal muscle cells by Ezh2 and DNA methylation mediated repression: Implications in duchenne muscular dystrophy. *PLoS One* **2010**, *5*, No. e12479.
(16) Robertson, K. D. DNA methylation and human disease. *Nat. Rev. Genet.* **2005**, *6*, 597−610.
(17) Cox, G. F.; Bürger, J.; Lip, V.; Mau, U. A.; Sperling, K.; Wu, B.-L.; Horsthemke, B. Intracytoplasmic sperm injection may increase the risk of imprinting defects. *Am. J. Hum. Genet.* **2002**, *71*, 162−164.
(18) Manning, M.; Lissens, W.; Bonduelle, M.; Camus, M.; De Rijcke, M.; Liebaers, I.; Van Steirteghem, A. Study of DNA-methylation patterns at chromosome 15q11-q13 in children born after ICSI reveals no imprinting defects. *Mol. Hum. Reprod.* **2000**, *6*, 1049−1053.
(19) Mishina, Y.; Duguid, E. M.; He, C. Direct reversal of DNA alkylation damage. *Chem. Rev.* **2006**, *106*, 215−232.
(20) Wyatt, M. D.; Pittman, D. L. Methylating agents and DNA repair responses: Methylated bases and sources of strand breaks. *Chem. Res. Toxicol.* **2006**, *19*, 1580−1594.
(21) Bignami, M.; O'Driscoll, M.; Aquilina, G.; Karran, P. Unmasking a killer: DNA O6-methylguanine and the cytotoxicity of methylating agents. *Mutat. Res., Rev. Mutat. Res.* **2000**, *462*, 71−82.
(22) Loechler, E. L.; Green, C. L.; Essigmann, J. M. In vivo mutagenesis by O6-methylguanine built into a unique site in a viral genome. *Proc. Natl. Acad. Sci. U.S.A.* **1984**, *81*, 6271−6275.
(23) Kelley, M. R.; Fishel, M. L. *DNA Repair in Cancer Therapy: Molecular Targets and Clinical Applications*; Acdemic Press: USA, 2016.
(24) Cao, J.; Jin, S.; Han, B.; Liu, W.; Zhao, L.; Zhong, R. DFT studies on the quantitative structure-activity relationship of *N*-(2-chloroethyl)-*N*′-cyclohexyl-*N*-nitrosoureas as anticancer agents. *Proceedings of the 3rd International Conference on Biomedical Engineering and Informatics, Yantai, China*, Oct 16−18, 2010.
(25) Mitra, S. MGMT: A personal perspective. *DNA Repair* **2007**, *6*, 1064−1070.
(26) Shukla, P. K.; Mishra, P. C.; Suhai, S. Reactions of DNA bases with the anti-cancer nitrogen mustard mechlorethamine: A quantum chemical study. *Chem. Phys. Lett.* **2007**, *449*, 323−328.
(27) Shukla, P. K.; Mishra, P. C. A quantum chemical study of reactions of DNA bases with sulphur mustard: A chemical warfare agent. *Theor. Chem. Acc.* **2009**, *125*, 269−278.
(28) Allay, E.; Veigl, M.; Gerson, S. L. Mice over-expressing human O6alkylguanine-DNA alkyltransferase selectively reduce O6methylguanine mediated carcinogenic mutations to threshold levels after N-methyl-N-nitrosourea. *Oncogene* **1999**, *18*, 3783.
(29) Kadlubar, F. F.; Beranek, D. T.; Weis, C. C.; Evans, F. E.; Cox, R.; Irving, C. C. Characterization of the purine ring-opened 7-methylguanine and its presistence in rat bladder epithelial DNA after treatment with the carcinogen N-methylnitrosourea. *Carcinogenesis* **1984**, *5*, 587−592.
(30) Swenberg, J. A.; Richardson, F. C.; Boucheron, J. A.; Dyroff, M. C. Relationships between DNA adduct formation and carcinogenesis. *Environ. Health Perspect.* **1985**, *62*, 177.
(31) Osborne, M. R.; Wilman, D. E. V.; Lawley, P. D. Alkylation of DNA by the Nitrogen Mustard Bis-(2-chloroethyl)methylamine. *Chem. Res. Toxicol.* **1995**, *8*, 316−320.
(32) Rinne, M. L.; He, Y.; Pachkowski, B.; Nakamura, J.; Kelley, M. R. N-methylpurine DNA glycosylase overexpression increases alkylation sensitivity by rapidly removing non-toxic 7-methylguanine adducts. *Nucleic Acids Res.* **2005**, *33*, 2859−2867.
(33) Fan, C.-H.; Liu, W.-L.; Cao, H.; Wen, C.; Chen, L.; Jiang, G. O6-methylguanine DNA methyltransferase as a promising target for the treatment of temozolomide-resistant gliomas. *Cell Death Dis.* **2013**, *4*, No. e876.
(34) Kaina, B.; Christmann, M.; Naumann, S.; Roos, W. P. MGMT: key node in the battle against genotoxicity, carcinogenicity and apoptosis induced by alkylating agents. *DNA Repair* **2007**, *6*, 1079−1099.
(35) Tubbs, J. L.; Pegg, A. E.; Tainer, J. A. DNA binding, nucleotide flipping, and the helix-turn-helix motif in base repair by O6-alkylguanine-DNA alkyltransferase and its implications for cancer chemotherapy. *DNA Repair* **2007**, *6*, 1100−1115.
(36) Pegg, A. E. Repair of O6-alkylguanine by alkyltransferases. *Mutat. Res., Rev. Mutat. Res.* **2000**, *462*, 83−100.
(37) Christmann, M.; Verbeek, B.; Roos, W. P.; Kaina, B. O6-Methylguanine-DNA methyltransferase (MGMT) in normal tissues and tumors: enzyme activity, promoter methylation and immunohistochemistry. *Biochim. Biophys. Acta, Rev. Cancer* **2011**, *1816*, 179−190.
(38) Kuo, K. C.; McCune, R. A.; Gehrke, C. W.; Midgett, R.; Ehrlich, M. Quantitative reversed-phase high performance liquid chromatographic determination of major and modified deoxyribonucleosides in DNA. *Nucleic Acids Res.* **1980**, *8*, 4763−4776.
(39) Kurdyukov, S.; Bullock, M. DNA methylation analysis: Choosing the right method. *Biology* **2016**, *5*, 3.
(40) Dahl, C.; Guldberg, P. DNA methylation analysis techniques. *Biogerontology* **2003**, *4*, 233−250.

DOI: 10.1021/acs.jpcc.8b10178
J. Phys. Chem. C XXXX, XXX, XXX−XXX

(41) Frommer, M.; McDonald, L. E.; Millar, D. S.; Collis, C. M.; Watt, F.; Grigg, G. W.; Molloy, P. L.; Paul, C. L. A genomic sequencing protocol that yields a positive display of 5-methylcytosine residues in individual DNA strands. *Proc. Natl. Acad. Sci. U.S.A.* **1992**, *89*, 1827−1831.
(42) Flusberg, B. A.; Webster, D. R.; Lee, J. H.; Travers, K. J.; Olivares, E. C.; Clark, T. A.; Korlach, J.; Turner, S. W. Direct detection of DNA methylation during single-molecule, real-time sequencing. *Nat. Methods* **2010**, *7*, 461−465.
(43) Eads, C. A.; Danenberg, K. D.; Kawakami, K.; Saltz, L. B.; Blake, C.; Shibata, D.; Danenberg, P. V.; Laird, P. W. MethyLight: A high-throughput assay to measure DNA methylation. *Nucleic Acids Res.* **2000**, *28*, 32e.
(44) Hu, J.; Zhang, C.-y. Single base extension reaction-based surface enhanced Raman spectroscopy for DNA methylation assay. *Biosens. Bioelectron.* **2012**, *31*, 451−457.
(45) Bell, S. E. J.; Sirimuthu, N. M. S. Surface-enhanced Raman spectroscopy (SERS) for sub-micromolar detection of DNA/RNA mononucleotides. *J. Am. Chem. Soc.* **2006**, *128*, 15580−15581.
(46) Li, H.; Sun, J.; Cullum, B. M. Label-free detection of proteins using SERS-based immuno-nanosensors. *NanoBiotechnology* **2006**, *2*, 17−28.
(47) Xu, L.-J.; Lei, Z.-C.; Li, J.; Zong, C.; Yang, C. J.; Ren, B. Label-free surface-enhanced Raman spectroscopy detection of DNA with single-base sensitivity. *J. Am. Chem. Soc.* **2015**, *137*, 5149−5154.
(48) Guerrini, L.; Krpetić, Ž.; van Lierop, D.; Alvarez-Puebla, R. A.; Graham, D. Direct Surface-Enhanced Raman Scattering Analysis of DNA Duplexes. *Angew. Chem.* **2014**, *127*, 1160−1164.
(49) Barhoumi, A.; Halas, N. J. Detecting chemically modified DNA bases using surface-enhanced Raman spectroscopy. *J. Phys. Chem. Lett.* **2011**, *2*, 3118−3123.
(50) Li, L.; Lim, S. F.; Puretzky, A.; Riehn, R.; Hallen, H. D. DNA Methylation Detection Using Resonance and Nanobowtie-Antenna-Enhanced Raman Spectroscopy. *Biophys. J.* **2018**, *114*, 2498−2506.
(51) Ouyang, L.; Hu, Y.; Zhu, L.; Cheng, G. J.; Irudayaraj, J. A reusable laser wrapped graphene-Ag array based SERS sensor for trace detection of genomic DNA methylation. *Biosens. Bioelectron.* **2017**, *92*, 755−762.
(52) Morla-Folch, J.; Xie, H.-n.; Gisbert-Quilis, P.; Pedro, S. G.-d.; Pazos-Perez, N.; Alvarez-Puebla, R. A.; Guerrini, L. Ultrasensitive Direct Quantification of Nucleobase Modifications in DNA by Surface-Enhanced Raman Scattering: The Case of Cytosine. *Angew. Chem.* **2015**, *127*, 13854−13858.
(53) Hu, P. P.; Liu, H.; Zhen, S. J.; Li, C. M.; Huang, C. Z. Nanosilver-based surface-enhanced Raman spectroscopic determination of DNA methyltransferase activity through real-time hybridization chain reaction. *Biosens. Bioelectron.* **2015**, *73*, 228−233.
(54) Wang, Y.; Zhang, C.-H.; Tang, L.-J.; Jiang, J.-H. Enzymatic control of plasmonic coupling and surface enhanced Raman scattering transduction for sensitive detection of DNA demethylation. *Anal. Chem.* **2012**, *84*, 8602−8606.
(55) Guerrini, L.; Krpetić, Ž.; van Lierop, D.; Alvarez-Puebla, R. A.; Graham, D. Direct Surface-Enhanced Raman Scattering Analysis of DNA Duplexes. *Angew. Chem., Int. Ed.* **2014**, *54*, 1144−1148.
(56) Wang, Y.; Wee, E. J. H.; Trau, M. Highly sensitive DNA methylation analysis at CpG resolution by surface-enhanced Raman scattering via ligase chain reaction. *Chem. Commun.* **2015**, *51*, 10953−10956.
(57) Kelly, J. G.; Martin-Hirsch, P. L.; Martin, F. L. Discrimination of base differences in oligonucleotides using mid-infrared spectroscopy and multivariate analysis. *Anal. Chem.* **2009**, *81*, 5314−5319.
(58) Kelly, J. G.; Najand, G. M.; Martin, F. L. Characterisation of DNA methylation status using spectroscopy (mid-IR versus Raman) with multivariate analysis. *J. Biophotonics* **2010**, *4*, 345−354.
(59) Chang, T.-W.; Gartia, M. R.; Seo, S.; Hsiao, A.; Liu, G. L. A wafer-scale backplane-assisted resonating nanoantenna array SERS device created by tunable thermal dewetting nanofabrication. *Nanotechnology* **2014**, *25*, 145304.
(60) Chang, T.-W.; Wang, X.; Mahigir, A.; Veronis, G.; Liu, G. L.; Gartia, M. R. Marangoni convection assisted single molecule detection with nanojet surface enhanced Raman spectroscopy. *ACS Sens.* **2017**, *2*, 1133−1138.
(61) Sundius, T. MOLVIB: A program for harmonic force field calculations. *QCPE Program*; Indiana University, 1991; p 604.
(62) Sundius, T. Molvib - A flexible program for force field calculations. *J. Mol. Struct.* **1990**, *218*, 321−326.
(63) Sundius, T. Scaling of ab initio force fields by MOLVIB. *Vib. Spectrosc.* **2002**, *29*, 89−95.
(64) Suh, J. S.; Moskovits, M. Surface-enhanced Raman spectroscopy of amino acids and nucleotide bases adsorbed on silver. *J. Am. Chem. Soc.* **1986**, *108*, 4711−4718.
(65) Lopes, R. P.; Marques, M. P. M.; Valero, R.; Tomkinson, J.; de Carvalho, L. A. E. B. Guanine: A combined study using vibrational spectroscopy and theoretical methods. *J. Spectrosc.* **2012**, *27*, 273−292.
(66) Zhao, L.-B.; Huang, Y.-F.; Liu, X.-M.; Anema, J. R.; Wu, D.-Y.; Ren, B.; Tian, Z.-Q. A DFT study on photoinduced surface catalytic coupling reactions on nanostructured silver: Selective formation of azobenzene derivatives from para-substituted nitrobenzene and aniline. *Phys. Chem. Chem. Phys.* **2012**, *14*, 12919−12929.
(67) Domke, K. F.; Zhang, D.; Pettinger, B. Tip-Enhanced Raman Spectra of Picomole Quantities of DNA Nucleobases at Au(111). *J. Am. Chem. Soc.* **2007**, *129*, 6708−6709.
(68) Madzharova, F.; Heiner, Z.; Gühlke, M.; Kneipp, J. Surface-enhanced hyper-raman spectra of adenine, guanine, cytosine, thymine, and uracil. *J. Phys. Chem. C* **2016**, *120*, 15415−15423.
(69) Fesenko, O.; Dovbeshko, G.; Dementjev, A.; Karpicz, R.; Kaplas, T.; Svirko, Y. Graphene-enhanced Raman spectroscopy of thymine adsorbed on single-layer graphene. *Nanoscale Res. Lett.* **2015**, *10*, 163.
(70) Merrick, J. P.; Moran, D.; Radom, L. An evaluation of harmonic vibrational frequency scale factors. *J. Phys. Chem. A* **2007**, *111*, 11683−11700.
(71) Scott, A. P.; Radom, L. Harmonic Vibrational Frequencies: An Evaluation of Hartree−Fock, Møller−Plesset, Quadratic Configuration Interaction, Density Functional Theory, and Semiempirical Scale Factors. *J. Phys. Chem.* **1996**, *100*, 16502−16513.
(72) Boysen, G.; Pachkowski, B. F.; Nakamura, J.; Swenberg, J. A. The formation and biological significance of N7-guanine adducts. *Mutat. Res., Genet. Toxicol. Environ. Mutagen.* **2009**, *678*, 76−94.
(73) Brookes, P.; Lawley, P. D. The reaction of mono- and di-functional alkylating agents with nucleic acids. *Biochem. J.* **1961**, *80*, 496.
(74) Singh, P.; Islam, S. S.; Ahmad, H.; Prabaharan, A. Spectroscopic investigation (FT-IR, FT-Raman), HOMO-LUMO, NBO, and molecular docking analysis of N -ethyl- N -nitrosourea, a potential anticancer agent. *J. Mol. Struct.* **2018**, *1154*, 39−50.
(75) Sapse, A. M.; Snyder, G.; Osorio, L. Self-consistent-field comparative studies of some nitrosoureas and nitrosamides. *Cancer Res* **1984**, *44*, 1904−1907.
(76) Montesano, R. Alkylation of DNA and tissue specificity in nitrosamine carcinogenesis. *J. Supramol. Struct. Cell. Biochem.* **1981**, *17*, 259−273.
(77) Beranek, D. T.; Weis, C. C.; Swenson, D. H. A comprehensive quantitative analysis of methylated and ethylated DNA using high pressure liquid chromatography. *Carcinogenesis* **1980**, *1*, 595−606.
(78) Shukla, P. K.; Mishra, P. C. Repair of O6-methylguanine to guanine by cysteine in the absence and presence of histidine and by cysteine thiolate anion: A quantum chemical study. *Phys. Chem. Chem. Phys.* **2009**, *11*, 8191−8202.
(79) Jerbi, J.; Springborg, M. Computational study of the reactivity of cytosine derivatives. *J. Comput. Chem.* **2017**, *38*, 1049−1056.
(80) Citti, L.; Gervasi, P. G.; Turchi, G.; Bellucci, G.; Bianchini, R. The reaction of 3, 4-epoxy-1-butene with deoxyguanosine and DNA in vitro: synthesis and characterization of the main adducts. *Carcinogenesis* **1984**, *5*, 47−52.

DOI: 10.1021/acs.jpcc.8b10178
J. Phys. Chem. C XXXX, XXX, XXX−XXX

(81) Margison, G. P.; Margison, J. M.; Montesano, R. Methylated purines in the deoxyribonucleic acid of various Syrian-golden-hamster tissues after administration of a hepatocarcinogenic dose of dimethylnitrosamine. *Biochem. J.* **1976**, *157*, 627−634.
(82) King, H. W. S.; Osborne, M. R.; Brookes, P. The in vitro and in vivo reaction at the N 7 -position of guanine of the ultimate carcinogen derived from benzo[a]pyrene. *Chem.-Biol. Interact.* **1979**, *24*, 345−353.
(83) Osborne, M.; Merrifield, K. Depurination of benzo[a]pyrene-diolepoxide treated DNA. *Chem.-Biol. Interact.* **1985**, *53*, 183−195.

DOI: 10.1021/acs.jpcc.8b10178
J. Phys. Chem. C XXXX, XXX, XXX−XXX